Modelling the Superpreading of Surfactant-laden Droplets with Computer Simulation

Panagiotis E. Theodorakis,[a] Erich A. Müller, [a] Richard V. Craster,[b] and Omar K. Matar[a]

Received Xth XXXXXXXXXX 20XX, Accepted Xth XXXXXXXXX 20XX
First published on the web Xth XXXXXXXXXX 200X
DOI: 10.1039/b000000x

The ability of certain surfactant molecules to drive the rapid wetting of hydrophobic substrates, known as superspreading, has been one of the most exciting research areas in surfactants during the last decades with applications ranging from coating technology to enhanced oil recovery. A key element of the superspreading mechanism is the adsorption of surfactant molecules from the liquid–vapour interface onto the substrate through the contact line, which must be coordinated with the replenishment of interfaces with surfactant from the interior of the droplet. Here, we find that these elements manifest themselves in various properties of the droplets, and we provide a detailed structural description of droplets during the superspreading process by using molecular dynamics simulations of a coarse-grained model. Additionally, we provide details on modelling surfactant-laden droplets, and propose an accurate method for estimating the contact angle of aqueous droplets. We anticipate that our study provides the fundamental knowledge to understand the basic features of the superspreading phenomenon relevant to many applications in engineering and medicine.

1 Introduction

Controlling the wetting of solid substrates by aqueous droplets, in view of many interesting applications, requires a fundamental understanding of spreading phenomena.[1–3] For instance, coating technology, enhanced oil recovery, drug delivery and herbicides are examples where control of wetting aims at enhancing the spreading ability of aqueous droplets on hydrophobic substrates.[4] The latter effect can be realised by using surfactants,[5] which reduce the free energy cost (interfacial tension) for the formation of interfaces (e.g., a liquid–vapour (LV) or a solid–liquid (SL) interface of a droplet) by preferentially adsorbing at the boundaries between different phases.[1] Although aqueous solutions containing surfactants are commonly used in many applications, a comprehensive understanding of the microscopic role of surfactant molecules in spreading phenomena remains challenging.[2–4,6] While experimental and theoretical studies have discussed possible mechanisms of spreading for surfactant-laden droplets,[2–4] molecular-scale simulations are indispensable for capturing the microcopic behaviour of surfactants associated with those mechanisms. To this end, molecular-level simulations[7] based on a coarse-grained force-field have recently unveiled the mechanism of superspreading,[6,8–11] which enables certain surfactants[12] to drive the anomalously fast[13] and complete wetting of moderately hydrophobic substrates.[9]

Previous work had initially focused on the study of aqueous and polymeric droplets on various technologically relevant substrates by using all-atom[14–17] and coarse-grained models.[18–34] However, the progress in computational capacity and the availability of reliable force-fields enabled the faithful modelling of surfactants in bulk aqueous solutions[35–41] suggesting links between the behaviour of surfactants in the bulk and their role in spreading processes.[42–45] In this context, the superspreading mechanism[12] and the main characteristics of superspreading surfactants have attracted much interest over the last years.[7,42–46] These studies have provided valuable information on the spreading of surfactant-laden droplets, but there are also aspects that require further discussion in order to complement our understanding of those phenomena. For example, such information includes details on identifying the different stages of the superspreading process, the dependence of the final contact area on surfactant concentration, the distribution of surfactant and water molecules in the bulk and at the interfaces of the droplet, or even a description of estimating reliably the macroscopic contact angle of aqueous droplets required for the parametrization of fluid–substrate interactions in a coarse-grained model.

In this study, we attempt to fill this gap by presenting results obtained by large-scale molecular dynamics (MD) simulations of a coarse-grained model implemented on general-purpose graphics processing units (GPGPUs) and applied for the study of the spreading of surfactant-laden aqueous droplets on substrates of moderate hydrophobicity (or wettability). Such sub-

[a] *Department of Chemical Engineering, Imperial College London, South Kensington Campus, London SW7 2AZ, United Kingdom*
[b] *Department of Mathematics, Imperial College London, South Kensington Campus, London SW7 2AZ, United Kingdom*

strates are characterized by a contact angle of water (CAW) around 60°, which is an optimum choice for the CAW as it corresponds to maximum values of spreading rate versus wettability for surfactant-laden droplets[9]. The force-field is based on a top-bottom coarse-graining approach, where the parameters are obtained from the Statistical Associating Fluid Theory (SAFT-γ).[47,48] The latter is an accurate equation of state (EoS), which provides a link between experimental macroscopic properties of a fluid and the underlying Hamiltonian. In this respect, we provide details of our coarse-graining approach. Furthermore, we discuss properties of a recently proposed single-site model[49] for water on solid planar substrates and trisiloxane surfactants and, also, discuss differences between aqueous nanodroplets of cylindrical and spherical cap geometries with theoretical arguments and a way of measuring CAW in simulations accurately. In addition, we compare our simulation model for water and Silwet-L77 surfactant with the experimental phase diagram as an example showing the faithfull representation of the fluid-fluid interactions using the SAFT force-field in bulk systems, which is key to simulating successfully superspreading experiments. Finally, we report on results of the superspreading of surfactant-laden droplets providing details of this phenomenon.[6,7]

2 Model and methods

2.1 Molecular dynamics simulations

Here, we use MD simulations of a coarse-grained model to study aqueous droplets. Henceforth, the Boltzmann constant is taken as unity and m and σ are the reduced units for the mass and the size of the beads, respectively, while ε defines the energy scale. Hence, the time unit is $\tau = \sigma(m/\varepsilon)^{1/2}$. Reduced and real units are related as follows: $\sigma = 0.43635$nm, $\varepsilon/k_B = 492$K, $m = 44.0521$amu, and the $\tau = 1.4062$ps. Care should be exercised with the literal interpretation of the time step. The coarse-graining procedure naturally removes some of the structural details of the models appearing 'smoother', hence increasing the effective diffusion coefficients. However, it is accepted that the coarse-grained models explore the phase space by roughly an order of magnitude faster than their atomistic counterparts.[50,51]

All simulations were carried out on GPGPUs by using the HOOMD package.[52] In addition, we have implemented the wall potential that describes the interactions between the fluid phase and the substrate[53] (Eq. 4). Moreover, the simulations were realised in the NVT ensemble by using the Nosé-Hoover thermostat as implemented in the HOOMD package, where the integration time step was $\Delta t = 0.005\tau$. The number of particles and the volume of the simulation box are constant during the simulations, while temperature fluctuates around a predefined value, $T = 0.6057$ (corresponding to $25°C$). For the aqueous droplets without surfactants the total number of water beads (N) in the simulation box varies from 2×10^3 to 24×10^4 beads. For the case of the aqueous droplets laden with surfactants, the total number of beads in the simulation box was always 8×10^4. The lengths of our trajectories for the surfactant-laden droplets depend on the time required for the spreading to complete (cf. Fig. 4c), when an equilibrium state establishes itself. In this case, typical trajectory lengths are between 10^7 and 10^8 MD time steps depending on the concentration of surfactant in the droplets. For the aqueous droplets without surfactants trajectories were 2×10^6 MD time steps after equilibration runs of up to 10^6 MD time steps depending on the size of the droplet. Trajectory samples were collected every 10^4 MD time steps for all cases, which guarantees the collection of independent statistical samples required for the analysis of the trajectories.

The simulation box for the spherical cap droplets, rectangular in shape, is 201σ long in the x and y directions, which guarantees that periodic images even of the largest droplet do not interact with each other due to the presence of periodic boundary conditions in these directions. In the z direction, beads were constrained by two walls normal to the z direction and parallel in the x and y directions. The distance between these two walls was typically 90σ for the droplets of the spherical cap geometry and 135σ for the cylindrical droplets. The bottom wall represents our substrate, which is unstructured and has infinite thickness described by a potential given below[53] (Eq. 4). The top wall is implemented as a purely repulsive potential and its distance from the bottom wall (substrate) guarantees that the top wall does not interact with any of the simulated droplets. Additionally, the size of the simulation box in the z direction is large enough to guarantee that the two walls do not interact with each other due to the presence of the periodic boundary conditions in the z direction. For cylindrical droplets, the length L (Fig. 1d) is along the y direction. In this direction, periodic boundary conditions apply, while in the z and x directions the simulation box is large enough to guarantee that mirror images of the droplet do not interact with each other in these directions.

2.2 Statistical Associating Fluid Theory (SAFT-γ)

The SAFT-γ is a molecular-based EoS that describes analytically the thermophysical data.[47] Due to the close match between the theory and the underlying Hamiltonian of a system, the EoS offers an accurate fit for the force-field parameters (parameters of the Mie potential[48]), which can be directly used in the simulations. Hence, the potential parameters are optimized to reproduce the macroscopically observed thermophysical properties and describe faithfully fluid–fluid and fluid–solid interactions. An overview of this top-down for obtaining coarse-grained potentials, is given in Ref.[47].

The derivation of robust and transferable potentials of effective beads may be combined to describe heterogeneous chain fluids.[54] This approach has shown promissing results in the simulation of complex fluids, for example, ethoxylated surfactants and photosensitive surfactants in water.[39,40] Furthermore, computer simulations using the SAFT-γ Mie force-field have successfully elucidated the superspreading mechanism of surfactant-laden droplets on hydrophobic substrates.[7] This methodology and the working equations have been discussed recently.[47,55,56]

2.3 Force-field

The nonbonded interactions between effective beads are described by the Mie potential. The parameters of the Mie potential were determined from the SAFT-γ EoS.[40,48,49] Each effective bead represents either a molecule, group of molecules or a chemical moiety and the parameters can all be traced to macroscopic properties of the original segments of pure components.[57] In our study, a bead denoted as 'W' represents two water molecules[49] (H_2O). Effective beads 'M' represent a chemical group $(CH_3)_3-Si-O_{\frac{1}{2}}$, and an effective bead 'D' corresponds to the group $O_{\frac{1}{2}}-(CH_3)_2-Si-O_{\frac{1}{2}}$. 'EO' effective beads represent $-CH_2-O-CH_2-$ (ether) chemical groups, while we make no distinction between terminal methyl groups and the CH_2 groups.[40] The masses of W, M, D, and EO effective beads are summarised in Table 1.

These beads interact via a Mie potential, which is mathematically described by the following relation,

$$U(r_{ij}) = C\varepsilon_{ij}\left[\left(\frac{\sigma_{ij}}{r_{ij}}\right)^{\lambda^r_{ij}} - \left(\frac{\sigma_{ij}}{r_{ij}}\right)^{\lambda^a_{ij}}\right] \quad (1)$$

where,

$$C = \left(\frac{\lambda^r_{ij}}{\lambda^r_{ij}-\lambda^a_{ij}}\right)\left(\frac{\lambda^r_{ij}}{\lambda^a_{ij}}\right)^{\left(\frac{\lambda^a_{ij}}{\lambda^r_{ij}-\lambda^a_{ij}}\right)}.$$

The indices i and j indicate the bead type (e.g., W, M, CM, etc.). Thus, σ_{ij}, ε_{ij}, λ^r_{ij}, and λ^a_{ij} are parameters of the Mie potential, while r_{ij} is the distance between any two beads. The values of Mie potential parameters for different pairs of beads are summarised in Table 2, while the cutoff is 4.5834σ. In addition, the parameter $\lambda^a_{ij} = 6$.

Surfactant molecules are built by binding effective beads with a harmonic potential, which is mathematically described as

$$V(r_{ij}) = 0.5k(r_{ij} - \sigma_{ij})^2, \quad (2)$$

where r_{ij} is again the distance between connected beads of type i and j, the values of σ_{ij} are given in Table 2, and $k = 295.33\varepsilon/\sigma^2$. Additionally, any three beads in each surfactant molecule of type EO interact via a harmonic angle potential

$$V_\theta(\theta_{ijk}) = 0.5k_\theta(\theta_{ijk} - \theta_0)^2, \quad (3)$$

where θ_{ijk} is the angle defined by three consecutive beads along the surfactant chain, $k_\theta = 4.32\varepsilon/rad^2$ is a constant, and $\theta_0 = 2.75rad$ is the equilibrium angle of the harmonic potential.

The fluid–substrate interactions were realised by an unbiased integration of the solid potential considering wall composed of spherical Mie beads.[53] Thus, the bottom wall in our case may represent an unstructured smooth substrate of infinite thickness. The form of the potential reads

$$U_{sub}(D) = 2\pi\rho C\varepsilon_{ij}\sigma^3_{ij}\left[A\left(\frac{\sigma_{ij}}{D}\right)^{\lambda^r_{ij}-3} - B\left(\frac{\sigma_{ij}}{D}\right)^{\lambda^a_{ij}-3}\right], \quad (4)$$

where $A = 1/(\lambda^r_{ij}-2)(\lambda^r_{ij}-3)$ and $B = 1/(\lambda^a_{ij}-2)(\lambda^a_{ij}-3)$. C, σ_{ij},ε_{ij}, λ^r_{ij}, and λ^a_{ij} have been defined in Eq. 1, ρ is the number density, which typically for a paraffinic substrate is $\rho \approx 1\sigma^{-3}$. D is the vertical distance between beads and the substrate. The cut-off of the fluid–substrate interaction

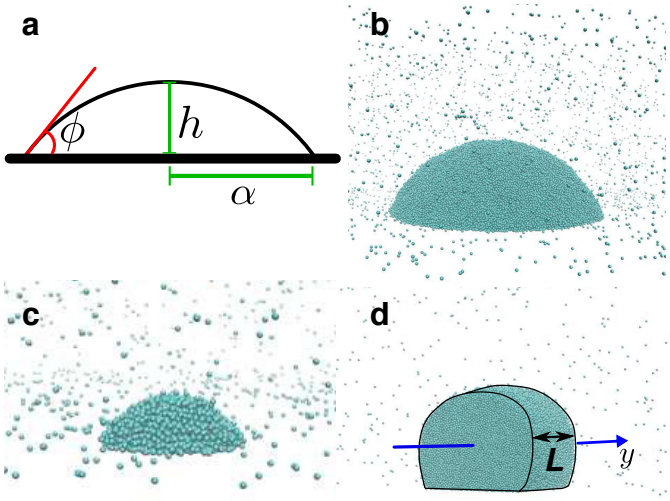

Fig. 1 (a) A cross-section of a spherical cap or cylindrical droplet, where the macroscopic contact angle ϕ, the height h and the radius α are indicated. Different snapshots of aqueous spherical cap (b,c) droplets on a hydrophilic substrate and a cylindrical droplet on a hydrophobic substrate ($\phi > \pi/2$) (d) are displayed. The length L is indicated in the case of cylindrical droplets (d). The simulation snapshots are not scaled in the figures according to their size for the sake of clarity. For example, in case (c) the droplet is zoomed in considerably compared to cases (b) and (d) in order to highlight the structure of the LV interface and the CL. The average size $\langle N \rangle$ of each droplet is approximately: 2×10^5 (b), 4×10^3 (c), and 8×10^4 (d) beads. In case (d) periodic boundary conditions are applied in the y direction.

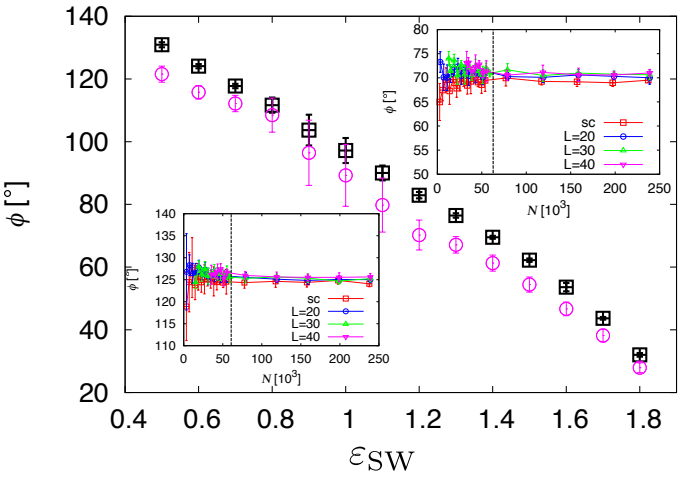

Fig. 2 Dependence of the contact angle on the substrate interaction ε_{SW} for a spherical cap droplet containing approximately on average 24×10^4 beads. Results have been obtained by appying Eq. 5 (squares) and a standard linear fitting method at the CL (circles). Insets illustrate the dependence of the contact angle ϕ based on Eq. 5 as a function of the average number of beads in the droplet $\langle N \rangle$ for a hydrophobic substrate (bottom left) and a hydrophilic susbstrate (top right) for spherical cap droplets (sc) and cylindrical droplets with $L = 20$,30, and 40 σ. The vertical line indicates an approximate limit over which ϕ does not depend on the average number of beads $\langle N \rangle$. Lines are a guide for the eye.

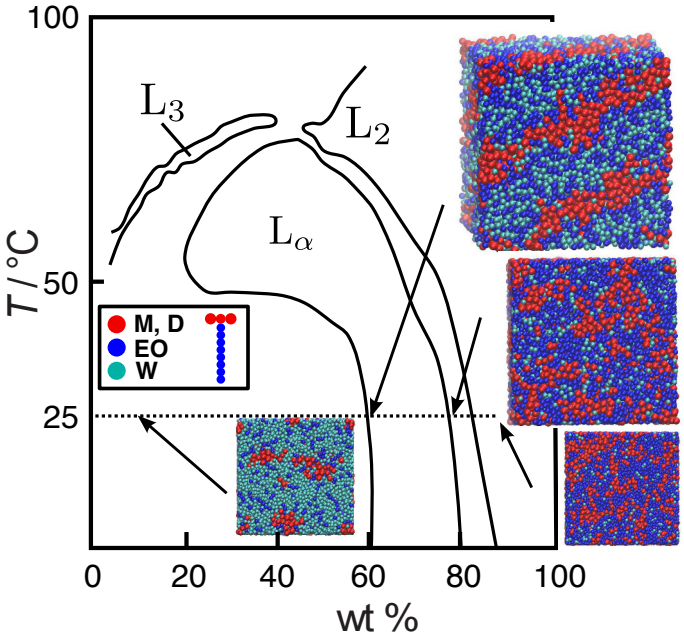

Fig. 3 Experimental phase diagram (Temperature vs. weight percent concentration [wt%]) for Silwet-L77. The experimental phase diagram has been adapted from Ref.[58]. Characteristic snapshots from the computer simulations based on the SAFT force field are also presented showing the characteristic fluid lamellar phase (L_α) in agreement with experiment. Colours indicate the type of beads as defined in the main text highlighting the distinction between surfactant hydrophobic beads (M, D), surfactant hydrophilic beads (EO), and water molecules (W). The T-shaped cartoon indicates the structure of the surfactant consisting of M-D-M beads (hydrophobic part) and eight EO (hydrophilic) beads, where the size of the beads is scaled according to their sizes (σ_{ii}) given in Table 2. Lines in the phase diagram do not indicate sharp phase boundaries as discussed in Ref.[58], in agreement with our simulations.

is the same with the cut-off used for the fluid–fluid interactions. The substrate–water (SW) interaction is tuned to provide a contact angle of approximately 60° by setting the value of $\varepsilon_{SW} = 1.4\varepsilon$ (cf., Fig. 2), from which one can obtain the substrate interaction parameter ε_{SS}. All other fluid–solid interactions arise from the use of common combination rules,[48] $\varepsilon_{ij} = (\sigma_{ii} + \sigma_{jj}/2)$, $\lambda^r_{ij} - 3 = \sqrt{(\lambda^r_{ii} - 3)(\lambda^r_{jj} - 3)}$, and $\varepsilon_{ij} = (1 - k_{ij})\sqrt{\sigma^3_{ii}\sigma^3_{jj}\varepsilon_{ii}\varepsilon_{jj}}/\sigma^3_{ij}$, where k_{ij} is an adjustable parameter.[7] The values of all parameters defining our force field have been briefly summarised in the appendix.

3 Results

3.1 Aqueous droplets and estimation of CAW

It is a common assumption that the curvature of the LV interface is the same along the LV interface of an aqueous droplet of either a spherical cap or a cylinder. However, this assumption might fail close to the contact line. Moreover, the equilibrium shape of the droplet is determined by the minimisation of the free energy, as expressed by the surface tensions and the corresponding interfacial areas; line tension can also contribute a term to the free energy, but this contribution is neglected in the present work.[59] Therefore, properties of the droplets, such as the macroscopic contact angle ϕ (Fig. 1a), may not depend on the size of the droplet (e.g., expressed by the average number of water molecules in our case) when all other conditions remain the same, e.g., thermodynamic conditions and the nature of interactions between different components and the substrate. Under the latter assumption, a different behaviour of properties as a function of droplet size will simply prove the invalidity of this assumption and will provide information on the minimum system size required for each property to asymptote to the macroscopic behaviour. Hence, the main assumption would be that droplets of different size will have the same shape independently of their size. This similarity in average equilibrium shape can be expressed by the ratio $\lambda = h/\alpha$ (Fig. 1a), where h is the vertical distance between the droplet apex and the SL interface, which we will refer to as 'droplet height', and α is the radius of the SL inter-

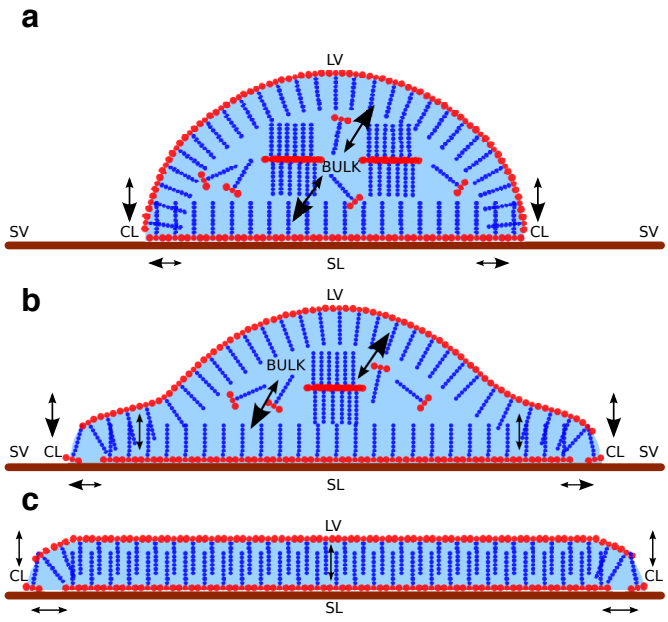

Fig. 4 Schematic illustration of a droplet cross-section and the leading adsorption processes taking place during superspreading, initially (a), at an intermediate stage (b) and at the final equilibrium state (c). Each dynamic adsorption process is indicated by a different arrow, where the arrow end of larger size indicates the dominant direction of mass transport, while the overall size of the arrows typifies the absolute magnitude of this adsorption process. Namely, the main adsorption processes of the superspreading mechanism are the hopping of surfactant from the LV to the SL interface through the contact line (CL), and the replenishment of surfactant at the interfaces (SL and LV) with surfactant coming from the bulk. The final stage is a bilayer (thin film), where surfactant molecules at liquid–vapour (LV) and solid–liquid (SL) interfaces are in dynamic equilibrium. Figure adapted from Ref.[7].

face, which we will simply refer to as 'droplet radius'. In the following, we express properties of the droplets as a function of the ratio λ, which describes the similarity between droplets of different size.

By using standard mathematical treatment,[60] the contact angle ϕ is

$$\phi = \arcsin(1/\mu), \tag{5}$$

for hydrophilic substrates ($\phi < \pi/2$) for both cylindrical and spherical cap droplets, where $\mu = (1+\lambda^2)/(2\lambda)$. Hence, droplets of different size will have the same contact angle ϕ, given that the ratio λ is the same. For hydrophobic substrates the contact angle will be $\phi' = \pi - \phi$. Hence, it suffices to measure the average droplet height $\langle h \rangle$ and the average radius $\langle \alpha \rangle$ in order to determine the average value of the contact angle $\phi = \langle \phi \rangle$, namely the so-called Contact Angle of Water (CAW). Thus, the average value of the contact angle will be equivalent to the macroscopic contact angle accessible to continuum the-

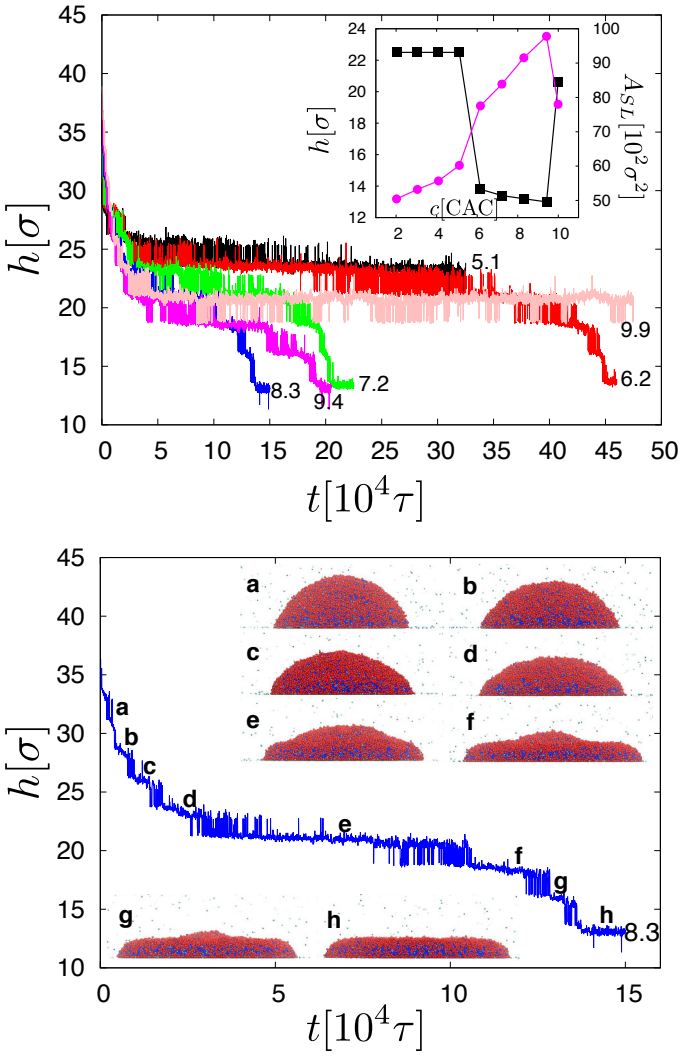

Fig. 5 Top panel: Height of the droplet as defined in the main text as a function of time for different concentrations as indicated. Inset displays the height (squares) and the final SL droplet area (circles) as a function of surfactant concentration. Lines are a guide for the eye. In the bottom panel, we chose the case of $c = 8.3$CAC, for which the fastest spreading occurs, in order to display simulation snapshots at different stages of the spreading process. Red colour corresponds to the hydrophobic moeities of Silwet-L77, blue to the hydrophilic groups, and cyan for water, the same as in Figs. 3 and 4. The scale of each snapshot is the same.

ory or experiment, because a fit within a certain fitting range of the LV interface at the CL is not required when using this method. Furthermore, we can measure the contact angle with remarkable accuracy in our simulations avoiding methodologies, which may include sophisticated fitting methods of the LV surface close to the CL, which, also, include a number of fitting parameters.[61]

In Fig. 2 we illustrate the dependence of the CAW ϕ on the interaction between water molecules and the solid substrate and we compare the above method of measuring the contact angle ϕ to a method using a linear fit applied on the LV interface close to the CL. In the case of the linear fit, the LV interface is determined by the most exterior beads belonging to the droplet, which are identified by a common cluster algorithm where the neighboring beads are $1.5\sigma_{ij}$ apart according to the Stillinger criterion,[62] as has been done previously.[7,63] Moreover, the fitting distance from the substrate to the LV interface should be large enough in order to describe the macroscopic trend of the contact angle, but, also simultaneously, small in order to comply with a linear assumption (linear fit) of the LV interface close to the CL. Of course, the latter compromise highlights perfectly only one of the general drawbacks of using fitting methods in order to measure the CAW.

Clearly, the calculation of the contact angle through the ratio λ overcomes the problems of fitting methods providing an accurate estimate of the CAW versus the substrate interaction $\varepsilon_{\rm SW}$, which in turn enables the evaluation of the parameter $\varepsilon_{\rm SS}$ of the substrate. The results of Fig. 2 indicate a linear dependence with the substrate interaction which diverges slightly only at small contact angles as manifested by the fitting and the method based on Eq. 5. This is expected, as the droplet height becomes comparable to the potential cut-off. Moreover, statistical errors are significantly lower in the case where Eq. 5 is applied in contrast to the results of the fitting method. These results refer to spherical cap aqueous droplet containing around 24×10^4 beads, for which the contact angle ϕ does not depend on the droplet size. As presented in the insets of Fig. 2, droplets containing more than approximately 6×10^4 have reached the macroscopic limit of the contact angle, and, hence, we expect that the results for ϕ presented in the main panel of Fig. 2 for droplets containing 24×10^4 beads are robust. The latter conclusion is valid irrespective of the substrate hydrophobicity (insets, Fig. 2). For droplets containing less than approximately 6×10^4 beads the contact angle depends on the size of the droplet, and statistical error bars are larger indicating also larger fluctuations in the dimensions of the droplets. Standard scaling analysis suggests that this limit is closer to 7×10^4 beads,[64] but an exact determination of this limit has not been possible. Furtermore, we have compared these results with the corresponding results based on a fitting method of estimating the contact angle ϕ, and we found strong dependence of ϕ on the size of the droplet, in agreement with previous simulation results.[61] Moreover, the line tension[59] does not seem to play a significant role, so as to change the behaviour of a droplet, in the case of large droplets. For small droplets, i.e., below 6×10^4 beads the role of the line tension may still be under debate.

In the following, we express properties of droplets as a function of droplet size through the ratio λ and the droplet radius α for aqueous droplets on hydrophilic substrates. Thus, the radius α indicates the 'size' of the droplet, while λ indicates the similarity between different droplets and does not vary with the droplet size given that thermodynamic conditions and the nature of interactions between water molecules and the substrate do not change. Hence, the scaling of droplet properties with their size should be expressed naturally through the radius α and the ratio λ, given that the macroscopic curvature along the LV is constant. For cylindrical droplets (Fig. 1c,d), $A^c_{LV}=2\alpha\mu L\phi$, $A^c_{SL}=2aL$, and $V^c=\alpha^2\nu L$, where ν depends only on the ratio λ, i.e., $\nu=\mu^2\phi-\mu\sqrt{1-(1/\mu)^2}$. μ and ϕ have been defined previously and L is the length of the cylindrical droplet (Fig. 1c,d). For droplets of spherical cap shape (Fig. 1b, c), $A^{sc}_{LV}=\alpha^2\pi(1+\lambda^2)$, $A^{sc}_{SL}=\alpha^2\pi$, and $V^{sc}=\alpha^3\pi\lambda(3+\lambda^2)/6$. These relations[65] clearly indicate that the computational cost of cylindrical droplets over spherical droplets scales as L/α. This means that for constant L the simulation of larger droplets (e.g., expressed through the droplet radius) becomes computationally more favorable, as the number of particles required for the molecular simulation of cylindrical droplets scales as as $N^{1/3}L/\alpha$, where N is the number of particles used in the simulation of a spherical-cap shaped droplet. Indeed, the values of contant angle ϕ for droplets with more than 6×10^4 beads are the same within the statistical error for cylindrical droplets of different L and spherical cap droplets justifying the use of cylindrical droplets in computer simulations given that the ratio L/α is chosen correctly. Hence, droplets over 6×10^4 can serve to set the CAW to its experimental value for different substrates. In this way, we have a reliable tool to extract the parameter $\varepsilon_{\rm SW}$ according to the experimental CAW, and, then extract the rest of the parameters for the cross-interaction parameters of surfactant molecules with the substrate based on the combining rules used in SAFT.[48] However, for droplets containing surfactants, it is still unclear whether cylindrical droplets should be favoured over spherical cap droplets regarding the spreading mechanisms. At first sight, there should be no apparent reason that this may happen in agreement with previous results.[44] Therefore, in the following we present results on spherical cap droplets containing Silwet-L77 surfactant, which is a superspreader.[6]

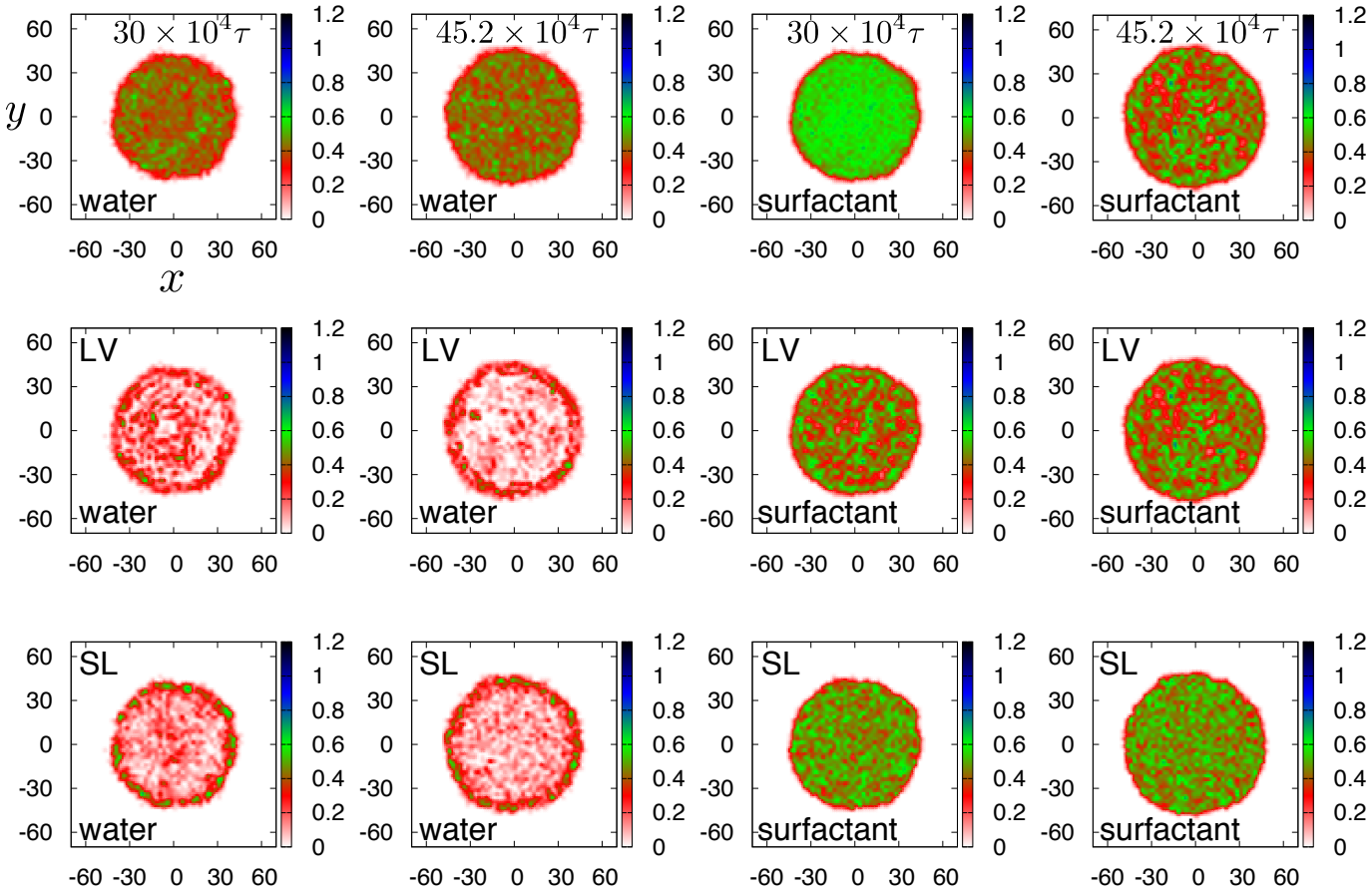

Fig. 6 Density of water or surfactant as indicated at the CWC (6.2CAC) seen from above (along the z direction) as a function of coordinates x and y. $0,0$ corresponds to the centre of the droplet. Density profiles have been calculated at the times shown for each column, i.e., an intermediate time corresponding to states such as that of Fig. 4b and a later time corresponding to states described schematically by Fig. 4c. The density profiles of water (two first columns) and surfactant molecules (two last columns) at the LV (second row) and SL (third row) interfaces are also indicated, while the first row contains results of the density at each x and y coordinates averaged all the way along the z direction.

3.2 Surfactant-laden droplets

3.2.1 Phase Behaviour of Silwet-L77 surfactant Simulations based on the SAFT force-field are able to describe the fluid–fluid interactions of surfactant aqueous solutions in the bulk. This is evidenced by the qualitative comparison of experimental phase behaviour[58] to the behaviour observed in our computer simulations (Fig. 3). In the case of Silwet-L77 surfactant, our model obtains the experimentally observed characteristic fluid lamellar (L_α) structure. Moreover, our simulations provide an overall qualitative description of the behaviour of this system. We have found that the ability of the SAFT force-field to reliably represent the fluid–fluid interactions between moieties and water molecules is indispensable to modelling the suprespreading mechanism to be discussed below. Similarly, the phase behaviour observed experimentally for C10E8 surfactant[66] (not shown here), which is a non-superspreading surfactant, agrees very well with our computer simulations based on the SAFT force-field, as well as in many other cases of nonanionic surfactants in aqeous solutions.[40] In this case, the characteristic hexagonal phase (cylinders) for high surfactant concentrations has been obtained from simulations in agreement with the experimental observation.[66] We have observed the formation of micellar-type structures at low to intermediate concentrations, while combinations of hexagonal and lamellar structures appear at higher surfactant concentration. Various phase diagrams based on the SAFT force field for other poly-alkyl-ether surfactants and details on the parameterization of these surfactant moeities validating the SAFT force-field have been recently provided.[40]

3.2.2 Superspreading Previously, we have elucidated the key elements of the superspreading mechanism by using MD

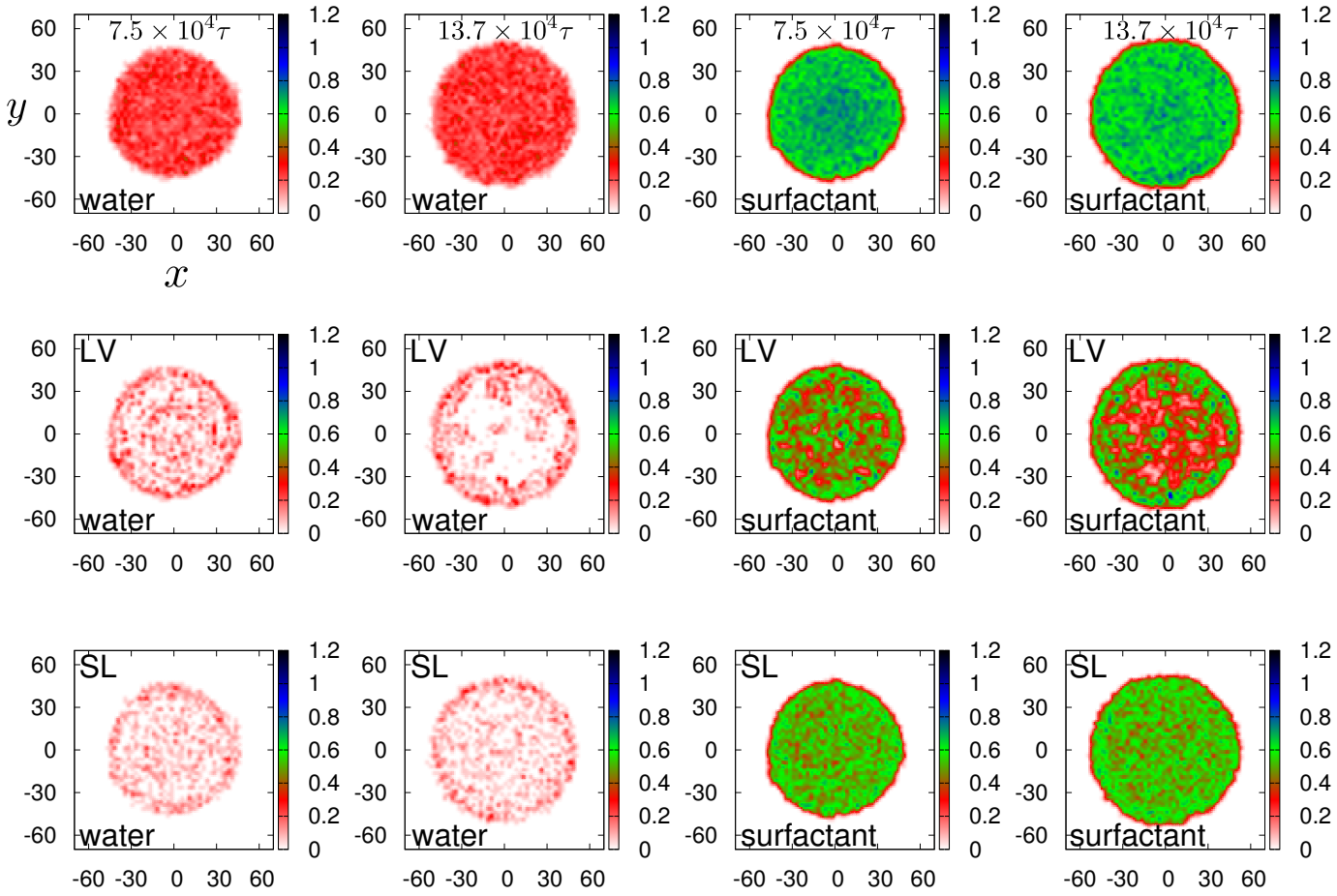

Fig. 7 Density of water or surfactant as indicated at the 8.3CAC on the plane normal to the z direction. $0,0$ corresponds to the centre of the droplet. Density profiles have been calculated at the times shown for each column, i.e., an intermediate time corresponding to states such as that of Fig. 4b and a later time corresponding to states described schematically by Fig. 4c. The density profiles of water (two first columns) and surfactant molecules (two last columns) at the LV (second row) and SL (third row) interfaces are also indicated, while the first row contains results of the density at each x and y coordinates averaged all the way along the z direction.

simulations of a coarse-grained model and analysing in detail the main adsorption mechanisms of this process[7] (Fig. 4). We have found that the first element of this mechanism is the adsorption of surfactant onto the substrate through the CL.[67] Crucially, this adsorption process must be followed by the replenishment of the LV and SL interfaces with surfactants coming from the interior of the droplet. At some incipient point, a bilayer forms at the CL and a rapid spreading process follows, as observed in experiments.[68,69] Also, we have found that the T-shape geometry favours the spreading process, which, in the case of superspreading surfactants, exhibits a maximum with the increase of surfactant concentration.[9] Manifestly, computer simulations have been able to capture this dependence recently for the first time.[7] Although the basic machanism is understood, it is now known that a plethora of different factors can suppress or aid superspreading behaviour, such as the rate of evaporation,[70] humidity,[9,71] pH,[72] surfactant structure and concentration,[73,74] surfactant aging effects,[75] surfactant mixtures,[76,77] substrate hydrophobicity,[9,71,78] and temperature.[71,79] However, it is not trivial to explain all these dependencies without a molecular perspective, hence the focus of this manuscript on some of the above aspects.

3.2.3 Discussion There are various properties of the droplet that enable a better understanding of superspreading. One of these properties is the droplet height h (cf. Fig. 1). We found that the height decreases gradually as a function of time (Fig. 5a). In the case of hydrophobic substrates, the hydrophobic moiety of surfactant attaches to the substrate increasing the size of the droplet in the planar directions. As a result, the height h of the droplet naturally decreases as the volume of the droplet remains the same. At this point, we observe that the droplet virtually oscillates between two states, until the replen-

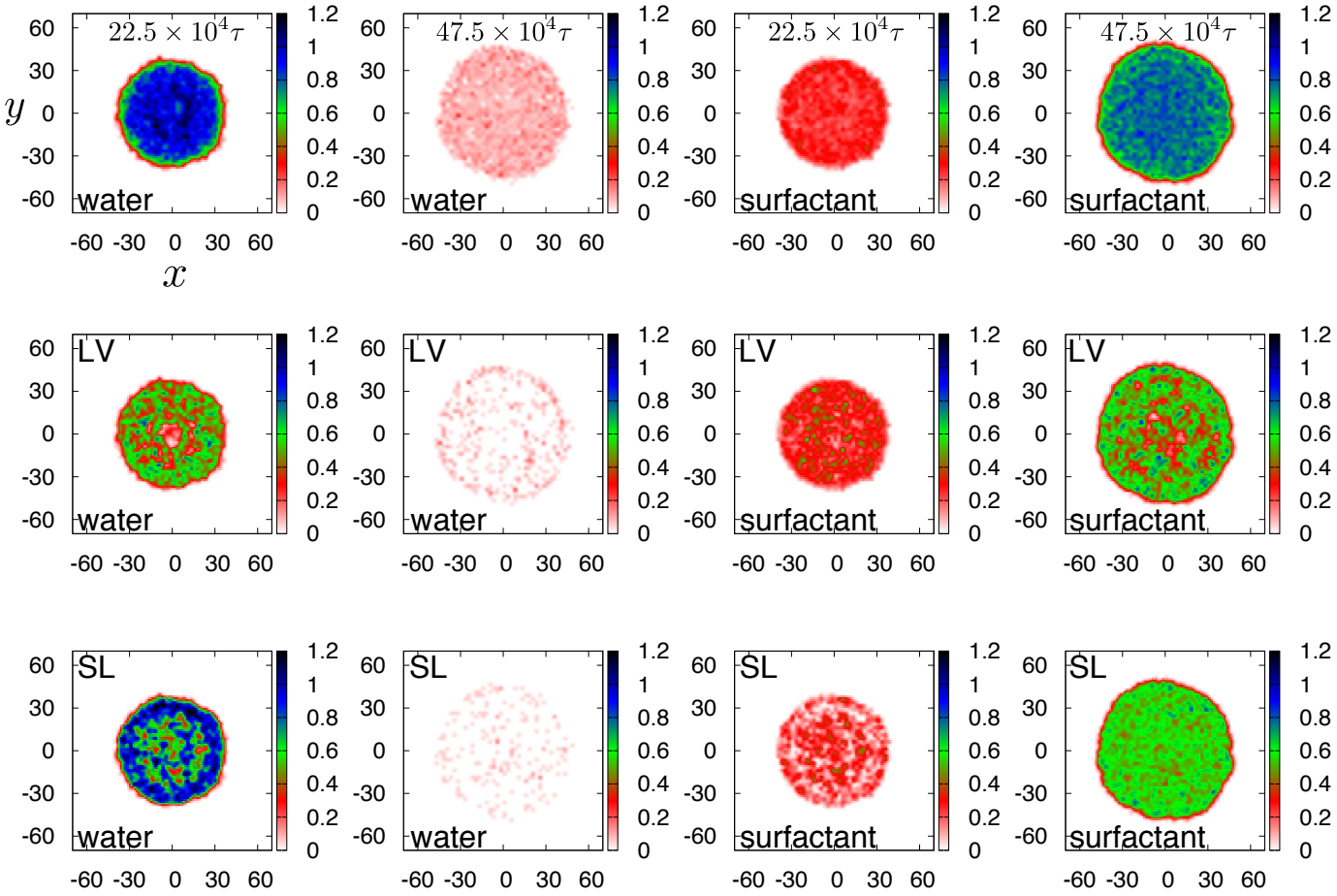

Fig. 8 Desnity profiles similar to Figs. 6 and 7 for a droplet having 2CAC surfactant concentration at time 22.5×10^4 and a droplet having 10CAC surfactant concentration at time 47.5×10^4. The first row presents results for the density at x, y averaged in the z directions, while the second and third rows display the density of water and surfactant at the LV and SL interfaces, respectively. The shape of the droplet in both cases resembles that of Fig. 4a.

ishment of the interfaces completes. Moreover, we observe that the time required for replenishment of interfaces with surfactant varies, while we can discern a prolonged intermediate state during the spreading (Fig. 5a). After the replenishment of the interfaces, the dragging process at the CL is facilitated due to the low surface tensions of the interfaces, resulting in the further increase of the droplet area. The whole process continues, until the occurrence of the thin film formation and the establishment of dynamic equilibrium (Fig. 4). Additionally, the spreading is faster and the height reduces more rapidly as surfactant concentration increases reaching an optimum value for certain concentration (Fig. 5a), for which, also, the maximum spreading rate as a function of concentration occurs.[7] Further increase of surfactant concentration results in a slower pace of decrease of the droplet height. For very high concentrations the surfactant reduces its superspreading ability (Fig. 5a), in agreement with experimental observations.[9]

The final values of droplet height, which are displayed in the inset of Fig. 5a indicate the same value of height within the statistical error for small surfactant concentrations, where the effect of surfactant is small. At a certain surfactant concentration, which is known as the Critical Wetting Concentration (CWC) we observe that the droplet height reduces dramatically (cf. Fig. 4c) reaching values which differ only slightly between each other. Further increase of surfactant concentration results in an abrupt increase of the droplet height, i.e., a deterioration of the spreading. On the other hand, the final area of the SL interface A_{SL} displays a smoother variation with surfactant concentration (inset of Fig. 5a). The latter may provide a hint that the height h of the droplet is related to the replenishment element of the superspreading mechanism, whereas the area may be a property closer linked to the adsorption of surfactant from the LV interface onto the substrate through the CL. Therefore, variations of the height h could provide an es-

timate of the time that surfactant molecules need to replenish the interfaces. Additionally, this time seems to be strongly correlated with the different stages of superspreading and the geometry of the LV interface (Fig. 5b). This may be evidenced by the appearance of the bilayer formation (cf. stage e of the droplet in Fig. 5b), where a dramatic change in the droplet geometry takes place, and up to the point that the spherical cap shape of the droplet starts to disappear into the thin film formation.

The fast pace of reduction in the droplet height in the latter stages of the droplet spreading (Fig. 5) may be explained by the small size of the droplet, which amounts only to a few tens of nanometres (e.g., from a droplet diameter of 30nm for the case of Fig. 4a to 60nm for the case of Fig. 4b[7]). This is also manifested by results on the density profiles (Figs. 6 and 7), which reveal the size and the shape of the droplet at a particular time corresponding to an intermediate state (cf. Fig. 4b) and a later time corresponding to the final equilibrium configuration of Fig. 4c or similar to that of Fig. 5f. Additionally, the spherical cap shape of the droplet at the region around droplet's apex, which tends to disappear as the spreading of droplet advances, results in a dramatic decrease of the droplet height at the latest stages of the spreading process, in agreement with the results of Fig. 5.

The water and surfactant molecules are homogenously distributed across the bulk of the droplet at any time during the spreading process, and the overall density of the droplets (water plus surfactant) also remains the same, as shown in Fig. 6 for a droplet at the CWC. However, by monitoring the surfactant at the LV interfaces (the dimension of each box element containing the interface beads is $2\sigma_{\mathrm{MM}}$) we observe that the amount of water molecules at the interfaces becomes smaller as water is 'sandwiched' between the LV and SL interfaces. The area close to the CL has a significant amount of water though, as it is exposed to the CL, where surfactant adsorbs directly from the LV interface onto the substrate. The same is true for the local density at the SL interface. Namely, water molecules are exposed to the vapour because of the formation of the bilayer, the adsorption from the LV onto the substrate through the CL, and the drag of water molecules from surfactant molecules at the CL area. Finally, we observe no pattern for the local density of surfactant molecules at any of the SL or LV interfaces, indicating that the geometry of the droplet during the spreading process does not affect the distribution of surfactant on these interfaces. This is observed at all times during the spreading process, and not only at the times indicated in Fig. 6. We only observe a small decrease in the density of surfactant at the LV interface, as the droplet assumes the more extended thin film conformation (Fig. 6), which becomes more apparent in the case of droplets with higher surfactant concentration (Fig. 7). For the latter case, similar effects are observed, but the patterns of the local density are more apparent in the case of the surfactant density profiles, clearly, due to the high concentration of surfactant.

The density profiles for droplets at low (2CAC) and high (10CAC) concentration (Fig. 8), namely below and above the CWC where spreading ability starts deteriorating significantly, differ considerably with the superspreading densities of Figs. 6 and 7. For low surfactant concentration, the LV interface has a higher density of water compared to the superspreading cases, despite being at a concentration two times higher than the Critical Aggregation Concentration (CAC). On the other hand, for high surfactant concentrations, the density profile of water at the LV interface shows a rather homogeneous structure than the ring pattern (higher density close to the LV interface) apparent in the superspreading regime (Fig. 8). Moreover, the density of surfactant at the LV interface in the case of low concentration (still above the CAC), is lower than the superspreading cases. For low concentrations, the SL interface is dominated by water molecules, while surfactant is much lower.

We have also monitored the time spent by each surfactant molecule at various regions of the droplets, i.e., the SL and LV intefaces, the CL, and the bulk. During the spreading of the droplets and for the superspreading cases, we have found that a significant amount of surfactant will visit the SL interface, while some of those surfactants will spend most of their time on this interface. The same is true for surfactants 'visiting' the LV interface. In this case, the probability of surfactants being at the LV interface is higher, because the LV interface can accomodate a larger number of surfactants than the SL inteface, and, also, surfactants at the LV interface have lower energy compared to the surfactants at the SL interface. However, at the CL only a small fraction of surfactants can spend up to 40% of their times at the CL during the spreading process. Finally, there are surfactants which will never become part of the bulk of the droplet, which is clearly, also, related to the small size of the simulated droplets. However, surfactants would prefer to become part of the interfaces, which in combination with the strong adsorption of surfactant onto the substates is the reason that such spreading processes occur in nature.

4 Summary and outlook

The rapid spreading of aqueous droplets on hydrophobic substrates, known as superspreading, has been an intensive field of research in view of important applications ranging from coating technology to enhanced oil recovery. A key element of the superspreading mechanism is the direct adsorption of surfactant molecules from the LV interface onto the substrate through the CL, which must be coordinated with the fast replenishment of the LV and the SL intefaces with surfactant

Table 1 The masses of M, D, W and EO effective beads in reduced mass units.

	W	M	D	EO
Mass [m]	0.8179	1.8588	1.6833	1.0000

from the interior of the droplet, while the formation of the bilayer at the CL is a constituent part of the mechanism.

We have discussed the modelling of surfatant-laden droplets in the context of superspreading. Starting from the discussion of a simple method of obtaining contact angles reliably at the macroscopic scale and extracting our parameters, we have identified the limit where the contact angle becomes independent of the droplet size for this model, in agreement with previous simulations studies.[61] We have also provided characteristic examples that validate the use of SAFT force fields in computer simulations as a coarse-graining tool that reproduces faithfully macroscopic properties. Moreover, we have discussed details of properties pertaining to the superspreading phenomenon providing details on the structural properties of the droplets during superspreading. We anticipate that this work elucidates the long-sought picture for the mechanism of superspreading, providing the fundamental background for industrial and medical applications.[6]

Acknowledgements

We gratefully acknowledge funding for our work provided by the Engineering and Physical Sciences Research Council (EPSRC), U.K., through grants EP/J010502, EP/I018212, EP/J014958, and EP/L020564. We express our gratitude to N. Kovalchuk and V. Starov from the University of Loughborough for fruitful discussions. We also thank Sadia Rahman for providing the SAFT parameters for the siloxane groups. The authors acknowledge support from the Thomas Young Centre under grant TYC-101. Our simulations were carried out at the GPGPU server in the Mathematics Department at Imperial College London.

5 Appendix

Here, we summarise the parameters used in our force-field as they are obtained by the SAFT-γ Mie EoS. The masses of the effective beads W, M, D, and EO are shown in Table 1. The values for the parameters of the Mie potential (cf., Eq. 1) are presented in Table 2.

Table 2 The parameters of the Mie potential for the interactions between beads. $\lambda_{ij}^{a} = 6$ in all cases.

i-j	$\sigma_{ij}[\sigma]$	$\varepsilon_{ij}[\varepsilon/k_B]$	λ_{ij}^{r}
W-W	0.8584	0.8129	8.00
W-M	1.0491	0.8132	13.72
W-D	0.9643	0.6311	10.38
W-EO	0.8946	0.9756	11.94
M-M	1.2398	0.8998	26.00
M-D	1.1550	0.7114	18.83
M-EO	1.0853	0.8262	22.18
D-D	1.0702	0.5081	13.90
D-EO	1.0004	0.6355	16.21
EO-EO	0.9307	0.8067	19.00

References

1 P.-G. deGennes, F. Brochard-Wyart and D. Quéré, *Capillarity and Wetting Phenomena: Drops, Bubbles, Pearls, Waves*, Springer, 2004.
2 D. Bonn, J. Eggers, J. Indekeu, J. Meunier and E. Rolley, *Reviews of Modern Physics*, 2009, **81**, 739–805.
3 R. V. Craster and O. K. Matar, *Reviews of Modern Physics*, 2009, **81**, 1131–1198.
4 O. K. Matar and R. V. Craster, *Soft Matter*, 2009, **5**, 3801–3809.
5 M. J. Rosen and J. T. Kunjappu, *Surfactants and Interfacial Phenomena*, John Wiley & Sons, New Jersey, 4th edn, 2012, p. 600.
6 P. E. Theodorakis, E. A. Müller, R. V. Craster and O. K. Matar, *Curr. Opin. Colloid Interface Sci.*, 2014, **19**, 283–289.
7 P. E. Theodorakis, E. A. Müller, R. V. Craster and O. K. Matar, *Langmuir*, 2015, **31**, 2304–2309.
8 E. G. Schwarz and W. G. Reid, *Ind. Eng. Chem.*, 1964, **56**, 26–35.
9 R. M. Hill, *Curr. Opin. Colloid Interface Sci.*, 1998, **3**, 247–254.
10 A. Nikolov and D. Wasan, *Eur. Phys. J.: Spec. Top.*, 2011, **197**, 325–341.
11 J. Venzmer, *Curr. Opin. Colloid Interface Sci.*, 2011, **16**, 335–343.
12 K. P. Ananthapadmanabhan, E. D. Goddard and P. A. Chandar, *Colloids Surf.*, 1990, **44**, 281–297.
13 S. Rafaï, S. Dipak, V. Bergeron, J. Meunier and D. Bonn, *Langmuir*, 2002, **18**, 10486–10488.
14 J. Hautman and K. M. L., *Phys. Rev. Lett.*, 1991, **67**, 1763–1766.
15 W. Mar and K. M. L., *J. Phys.: Condens. Matter*, 1994, **6**, A381–A388.
16 C. F. Fan and C. T., *J. Chem. Phys.*, 1995, **103**, 9053–9061.
17 J. M. D. Lane, M. Chandross, C. D. Lorenz, M. J. Stevens and G. S. Grest, *Langmuir*, 2008, **24**, 5734–5739.
18 G. Saville, *J. Chem. Soc., Faraday Trans. 2*, 1977, **73**, 1122–1132.
19 J. Sikkenk, J. Indekeu, J. van Leeuwen, E. Vossnack and A. Bakker, *J. Stat. Phys.*, 1988, **52**, 23–44.
20 M. Nijmeijer, C. Bruin, A. Bakker and J. V. Leeuwen, *Physica A: Statistical Mechanics and its Applications*, 1989, **160**, 166 – 180.
21 M. J. P. Nijmeijer, C. Bruin, A. F. Bakker and J. M. J. van Leeuwen, *Phys. Rev. A*, 1990, **42**, 6052–6059.
22 J. A. Nieminen and T. Ala-Nissila, *EPL (Europhysics Letters)*, 1994, **25**, 593.
23 J. A. Nieminen and T. Ala-Nissila, *Phys. Rev. E*, 1994, **49**, 4228–4236.
24 M. J. de Ruijter, T. D. Blake and J. De Coninck, *Langmuir*, 1999, **15**, 7836–7847.
25 T. Blake, A. Clarke, J. D. Coninck, M. de Ruijter and M. Voué, *Colloids and Surfaces A: Physicochemical and Engineering Aspects*, 1999, **149**, 123 – 130.
26 T. Blake, C. Decamps, J. D. Coninck, M. de Ruijter and M. Voué", *Colloids and Surfaces A: Physicochemical and Engineering Aspects*, 1999, **154**, 5 – 11.
27 M. Voué, S. Semal and J. De Coninck, *Langmuir*, 1999, **15**, 7855–7862.

28 M. Voué, S. Rovillard, J. De Coninck, M. P. Valignat and A. M. Cazabat, *Langmuir*, 2000, **16**, 1428–1435.
29 M. Voué and J. D. Coninck, *Acta Mater.*, 2000, **48**, 4405 – 4417.
30 J. D. Coninck, M. J. de Ruijter and M. Voué, *Current Opin. Colloid Interface Sci.*, 2001, **6**, 49 – 53.
31 M. Lundgren, N. L. Allan, T. Cosgrove and N. George, *Langmuir*, 2002, **18**, 10462–10466.
32 M. Lundgren, N. L. Allan, T. Cosgrove and N. George, *Langmuir*, 2003, **19**, 7127–7129.
33 D. R. Heine, G. S. Grest and E. B. Webb, *Phys. Rev. E*, 2003, **68**, 061603.
34 T. Werder, J. H. Walther, R. L. Jaffe, T. Halicioglu and P. Koumoutsakos, *J. Phys. Chem.*, 2003, **107**, 1345–1352.
35 M. S. Tomassone, A. Couzis, C. M. Maldarelli, J. R. Banavar and J. Koplik, *J. Chem. Phys.*, 2001, **115**, 8634–8642.
36 M. S. Tomassone, A. Couzis, C. M. Maldarelli, J. R. Banavar and J. Koplik, *Langmuir*, 2001, **17**, 6037–6040.
37 W. Shinoda, R. DeVane and M. L. Klein, *Molecular Simulation*, 2007, **33**, 27–36.
38 W. Shinoda, R. DeVane and M. L. Klein, *Soft Matter*, 2008, **4**, 2454–2462.
39 C. Herdes, E. E. Santiso, C. James, J. Eastoe and E. A. Müller, *J. Colloid Interface Sci.*, 2015, **445**, 16–23.
40 O. Lobanova, *PhD thesis*, Imperial College London, 2014.
41 R. E. Isele-Holder and A. E. Ismail, *J. Phys. Chem. B*, 2014, **118**, 9284–9297.
42 Y. Shen, A. Couzis, J. Koplik, C. Maldarelli and M. S. Tomassone, *Langmuir*, 2005, **21**, 12160–12170.
43 H.-Y. Kim, Q. Yin and K. A. Fichthorn, *J. Chem. Phys.*, 2006, **125**, 174708.
44 J. D. Halverson, C. Maldarelli, A. Couzis and J. Koplik, *Chem. Eng. Sci.*, 2009, **64**, 4657–4667.
45 D. Sergi, G. Scocchi and A. Ortona, *J. Chem. Phys.*, 2012, **137**, 094904.
46 R. E. Isele-Holder, B. Berkels and A. E. Ismail, *Soft Matter*, 2015, **11**, 4527–4539.
47 E. A. Müller and G. Jackson, *Annu. Rev. Chem. Biomol. Eng.*, 2014, **5**, 405–427.
48 T. Lafitte, A. Apostolakou, C. Avendaño, A. Galindo, C. S. Adjiman, E. A. Müller and G. Jackson, *J. Chem. Phys.*, 2013, **139**, 154504.
49 O. Lobanova, C. Avendaño, T. Lafitte, E. A. Müller and G. Jackson, *Mol. Phys.*, 2015, **113**, 1228–1249.
50 S. J. Marrink, H. J. Risselada, S. Yefimov, D. P. Tieleman and A. H. de Vries, *J. Phys. Chem. B*, 2007, **111**, 7812–7824.
51 A. Brini, E. A. Algaer, P. Ganguly, C. Li, F. Rodrguez-Ropero and van der Vegt N. F. A., *Soft Matter*, 2013, **9**, 2108–2119.
52 J. A. Anderson, C. D. Lorenz and A. Travesset, *J. Comput. Phys.*, 2008, **227**, 5342–5359.
53 E. Forte, A. J. Haslam, G. Jackson and E. A. Müller, *Phys. Chem. Chem. Phys.*, 2014, **16**, 19165–19180.
54 V. Papaioannou, T. Lafitte, C. Avendaño, C. S. Adjiman, G. Jackson, E. A. Müller and A. Galindo, *J. Chem. Phys.*, 2014, **140**, 054107.
55 C. Avendaño, T. Lafitte, A. Galindo, C. S. Adjiman, G. Jackson and E. A. Müller, *J. Phys. Chem B*, 2011, **115**, 11154–11169.
56 C. Avendaño, T. Lafitte, A. Galindo, C. S. Adjiman, E. A. Müller and G. Jackson, *J. Phys. Chem B*, 2013, **117**, 2717–2733.
57 A. Mejía, C. Herdes and E. A. Müller, *Ind. Eng. Chem. Res.*, 2014, **53**, 4131–4141.
58 R. M. Hill, M. He, H. T. Davis and L. E. Scriven, *Langmuir*, 1994, **10**, 1724–1734.
59 J. H. Weijs, A. Marchand, B. Andreotti, D. Lohse and J. H. Snoeijer, *Phys. Fluids*, 2011, **23**, 022001.
60 F. Leroy and F. Müller-Plathe, *J. Chem. Phys.*, 2010, **133**, 044110.
61 E. E. Santiso, C. Herdes and E. A. Müller, *Entropy*, 2013, **15**, 3734–3745.
62 F. H. Stillinger, *J. Chem. Phys.*, 1963, **38**, 1486.
63 P. E. Theodorakis, W. Paul and K. Binder, *J. Chem. Phys.*, 2010, **133**, 104901.
64 O. Melchert and A. K. Hartmann, *Phys. Rev. B*, 2009, **79**, 184402.
65 J. W. Harris and H. Stocker, *Handbook of Mathematics and Computational Science*, Springer Verlag, New York, 1998.
66 Y. Nibu and T. Inoue, *J. Colloid Interface Sci.*, 1998, **205**, 305–315.
67 G. Karapetsas, R. V. Craster and O. K. Matar, *J. Fluid Mech.*, 2011, **670**, 5–37.
68 F. Tiberg and C.-M. Cazabat, *Europhys. Lett.*, 1994, **25**, 205–210.
69 E. Ruckenstein, *Colloids Surf., A*, 2012, **412**, 36–37.
70 S. Semenov, A. Trybala, H. Agogo, N. Kovalchuk, F. Ortega, R. G. Rubio, V. M. Starov and M. G. Velarde, *Langmuir*, 2013, **29**, 10028–36.
71 N. A. Ivanova, Z. B. Zhantenova and V. M. Starov, *Colloids Surf., A*, 2012, **413**, 307–313.
72 J. Radulovic, K. Sefiane and M. E. Shanahan, *J. Colloid Interface Sci.*, 2009, **332**, 497–504.
73 N. Ivanova, V. Starov, R. Rubio, H. Ritacco, N. Hilal and D. Johnson, *Colloids Surf., A*, 2010, **354**, 143–148.
74 T. Svitova, R. M. Hill, Y. Smirnova, A. Stuermer and G. Yakubov, *Langmuir*, 1998, **14**, 5023–5031.
75 J. Radulovic, K. Sefiane and M. E. R. Shanahan, *Chem. Eng. Sci.*, 2010, **65**, 5251–5255.
76 M. J. Rosen and Y. Wu, *Langmuir*, 2001, **17**, 7296–7305.
77 M. J. Rosen and Y. Wu, *Langmuir*, 2002, **18**, 2205–2215.
78 J. Radulovic, K. Sefiane and M. E. R. Shanahan, *J. Bionic Eng.*, 2009, **6**, 341–349.
79 N. A. Ivanova and V. M. Starov, *Curr. Opin. Colloid Interface Sci.*, 2011, **16**, 285–291.